ARMA 17-0642

Simulation of refracture and contact mode transitions in tight formations

Abedi, R., Clarke, P.L,
Department of Mechanical, Aerospace & Biomedical Engineering, The University of Tennessee Space Institute, TN, USA

ABSTRACT: Transitions between separation and contact modes are prevalent in rock mechanics. For stimulating tight hydrocarbon reservoirs, the transfer of hydraulic load from hydraulically loaded to in-situ cracks, removal of hydraulic load, re-fracturing, and application of cyclic loading are all examples involving contact and separation mode reversal. We propose an interfacial damage model that incorporates all contact and separation modes by combining their corresponding dynamically consistent Riemann solutions. Instead of commonly used penalty method and Lagrange multiplier approach we propose a new regularization scheme—based on the interface displacement and separation velocity jumps—that smoothens contact-separation mode transitions, remedies ill-conditioning that may arise by using penalty methods, and provides a tunable maximum penetration. In addition, we propose an aperture-based regularization approach that enables smooth transfer of hydraulic load to in-situ cracks. Numerical results, obtained by an h-adaptive spacetime discontinuous Galerkin method, demonstrate accurate modeling of contact mode transitions and intersection of cracks in hydraulic fracturing.

1 INTRODUCTION

Given that rocks are often under confinement pressure, contact and friction play a critical role in rock mechanics. For problems involving crack propagation and intersection, transitions between separation, contact–stick, and contact–slip may occur. There are specifically several examples in the area of hydrocarbon reservoir characterization and stimulation. In hydraulic fracturing the interaction of a hydraulically loaded crack with in-situ cracks can result in various mode transitions for both cracks. For example, the hydraulically loaded crack can be arrested or change direction by the in-situ crack or penetrate through it. The fluid flow can also be diverted into the in-situ crack, in which case it experiences a contact to separation mode transition; *cf.* [1] for the review of such intersections and the types of mode transitions that may be involved.

The inverse of the aforementioned mode transition, *i.e.,* separation to contact mode transition, occurs when the hydraulic load is released and crack surface are pulled back together. Understanding this transition, and the transition back to separation mode due to the re-application of hydraulic load becomes important in refracting applications; cyclic application of the loads that better stimulate a reservoir, as in [2,3], or re-fracturing a reservoir to reactivate hydraulic cracks or increase its productivity, *cf.* [4], are some applications that involve contact mode transitions.

The most common numerical techniques for contact include *penalty methods* [5,6] and *Lagrange multiplier methods* [7,8] In the context of rock mechanics and hydraulic fracturing [3,9] use the cohesive model approach to represent fracture processes on crack surfaces. To model contact, the former employs a penalty method while the latter enforces the contact condition by using a Lagrange multiplier approach. It is noted that penalty methods allow an unpredictable amount of interpenetration and can generate stiff, ill-conditioned systems that might require extremely small time steps for stability [10].

The contact formulation in [11] remedies the uncontrollable penetration of penalty methods by providing a maximum tunable penetration without resulting in a stiff system of equations. This approach is naturally formulated for dynamic problems by formulating and combining local Riemann solutions from various contact modes. However, in its present form it cannot be applied to hydraulic fracturing applications as it does not correctly model contact–stick to separation mode transitions. In the present work, we propose a new regularization approach in the two dimensional phase space of normal separation and normal separation velocity jump that remedies this problem, *cf.* §2.2.2. Another aspect that is addressed in the present work is the contact to separation mode transition encountered upon the intersection of a hydraulically loaded crack with an in-situ crack. We propose an aperture-based approach to regularize the application of hydraulic load to newly loaded crack segments. The proposed dynamic contact conditions are incorporated in an interfacial damage model. This contact / fracture model is used for the simulation of hydraulic crack propagation and intersection problems and a simplified re-fracture problem in §3.

2 FORMULATION

In this section we provide the formulation of an interfacial damage model that also incorporates dynamically consistent solutions for contact–stick and contact–slip modes. Cohesive models are commonly used to represent nonlinear material responses on a fracture surface. However, the enforcement of impenetrability condition and Coulomb friction relation is challenging for cohesive models. In lieu of a cohesive model, we represent the process of material degradation on a fracture surface by an interfacial damage parameter D that ranges from zero for a fully bonded interface to $D = 1$ for a fully debonded one. There are two key components to the damage model. First, given the traction and velocity states on the two sides of an interface, dynamically consistent solutions for various contact modes are obtained by the solution of local Riemann problems in §2.1. Second as described in §2.2, by determining which mode(s) are active on a given point on a contact/fracture interface, we linearly combine the aforementioned Riemann solutions to derive macroscopic traction and velocity solutions. These macroscopic target solutions replace the *traction separation relation* (TSR) that is used in the context of cohesive models by specifying the traction (and velocity) state of the interface based on the traces of the solution from the opposite sides of the interface. Finally, in §2.3 we describe the process to smoothly apply hydraulic pressure on newly connected fracture surfaces to hydraulically loaded and propagating fracture network. Contact/separation model transitions in hydraulic fracturing are also described in §2.3.

2.1 Riemann solutions for different contact modes

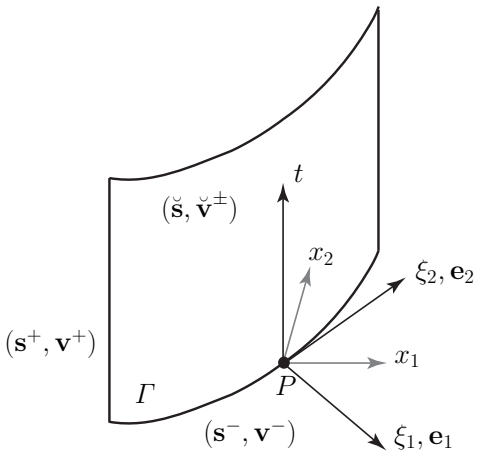

Figure 1: Local coordinate frame at arbitrary spacetime location P on a spacetime fracture surface Γ for a problem in two spatial dimensions.

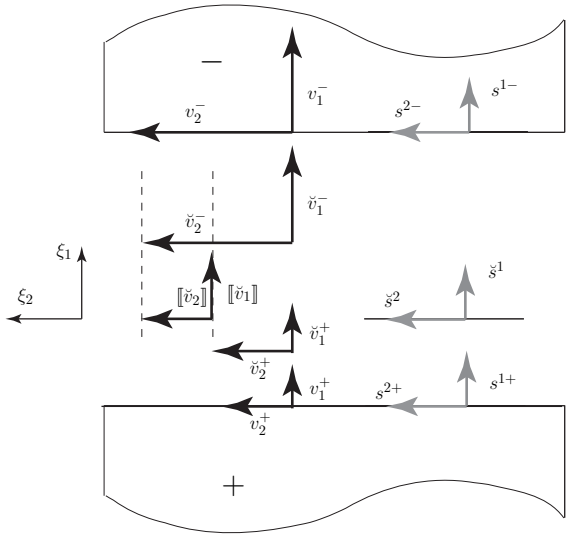

Figure 2: Top zoomed view of the point P from fig. 1. While the target traction solutions are the same $\breve{\mathbf{s}}^+ = \breve{\mathbf{s}}^- := \breve{\mathbf{s}}$, depending on a given contact mode kinematic compatibility, normal and tangential components of target velocities, $\breve{\mathbf{v}}^+$ and $\breve{\mathbf{v}}^-$, can be distinct from the two sides.

For completeness, this section provides a short overview of different Riemann contact solutions from [11] with an improved and modified notation. Bonded, contact–stick, contact–slip, and separation are collectively called contact modes. The solutions for individual contact modes are obtained by solving local Riemann problems at a contact interface. A local coordinate frame at an arbitrary spacetime location P on contact interface Γ is illustrated in fig. 1. The local coordinates are (ξ_1, ξ_2, t), and the frame is oriented such that the ξ_1-direction aligns with the spatial normal vector on Γ from + to − sides. The quantities from the opposite sides of Γ, which are decorated with superscripts + and −, define the initial data for the Riemann problem. Distinct velocity traces, $\mathbf{v}^{\pm}$, and tractions, $\mathbf{s}^{\pm}$, from the traces of solution fields from the two sides. Tractions are defined by $\mathbf{s} = \boldsymbol{\sigma} \cdot \mathbf{n}$ in which the same spatial normal vector, $\mathbf{n}$, is used to compute $\mathbf{s}^+$ and $\mathbf{s}^-$. The Riemann values at a given point P on the interface include components of the traction vector acting on the interface and traces of the velocity components from each side of the interface. We denote these by $(\breve{\mathbf{s}}, \breve{\mathbf{v}}^{\pm})$, as shown in the figure. Balance of linear momentum requires equality between the traction vectors obtained from the stress fields on opposite sides of the interface. That is, $\breve{\mathbf{s}}^+ = \breve{\mathbf{s}}^- := \breve{\mathbf{s}}$.

The kinematic compatibility conditions on the interface depend on whether the material interface is intact (perfectly bonded), or in the debonded case, on the specific contact mode. The target velocities on Γ are equal for bonded and contact–stick cases. For contact–slip case, while the impenetrability condition implies the continuity of target velocities in normal direction, $\breve{v}_1^+ = \breve{v}_1^-$, the tangential components can be discontinuous due to slip condition. Finally, in separation model, all components of $\breve{\mathbf{v}}^+$ and $\breve{\mathbf{v}}^-$ can be discontinuous. Figure 2 shows a top

and zoomed view for the point P in fig. 1. Interior traces of the solution are shown on the two sides of the interface and target values between the two sides. As evident, unlike target tractions, target velocities can be discontinuous and $[\![\breve{\mathbf{v}}]\!]$ denotes the corresponding jump.

The Riemann solutions are obtained by preserving the characteristic values of the elastodynamic problem and enforcing kinematic conditions pertinent to a given contact mode. For an isotropic material in linear elastodynamics, the spacetime characteristic trajectories in all directions are determined by the dilatational and shear wave speeds, $c_d^{\pm}$ and $c_s^{\pm}$,

$$c_{\mathrm{d}} = \sqrt{\frac{\lambda + 2\mu}{\rho}}, \qquad c_{\mathrm{s}} = \sqrt{\frac{\mu}{\rho}}. \tag{1}$$

where ρ is the mass density and λ, μ are the Lamé parameters.

The definition of characteristic values, [11], uses the impedance values given by,

$$Z^{i\pm} := \begin{cases} (c_d\rho)^{\pm} & i = 1 \\ (c_s\rho)^{\pm} & i = 2,3 \end{cases} \tag{2}$$

in which the index i corresponds to spatial directions in the local frame shown in fig. 1.

After the solution of the local Riemann, the target values for contact–stick and bonded modes decorated with ST and B respectively, are obtained as,

$$\breve{s}^i_{\mathrm{B}} = \breve{s}^i_{\mathrm{ST}} = \breve{s}^i = \frac{s^{i+}Z^{i-} + s^{i-}Z^{i+}}{Z^{i-} + Z^{i+}} + \frac{Z^{i-}Z^{i+}}{Z^{i-} + Z^{i+}}(v_i^+ - v_i^-) \tag{3a}$$

$$\breve{v}_{\mathrm{B}_i} = \breve{v}_{\mathrm{ST}_i} = \breve{v}_i = \frac{s^{i-} - s^{i+}}{Z^{i-} + Z^{i+}} + \frac{v_i^+ Z^{i+} + v_i^- Z^{i-}}{Z^{i-} + Z^{i+}} \tag{3b}$$

the index i ranges from 1 to d the spatial dimension of the problem. No summation convention is implied for repeated index i. The quantities (s^{i+}, v_i^+) and (s^{i-}, v_i^-) are shown in fig. 2 for a 2D ($d = 2$) geometry. As expected from (3b), we have $\breve{\mathbf{v}}^+ = \breve{\mathbf{v}}^- := \breve{\mathbf{v}}$.

In separation mode, $\breve{\mathbf{v}}^+$ and $\breve{\mathbf{v}}^-$ are fully independent. The Riemann tractions are, however, set equal to $\mathbf{S}$, the tractions specified by a particular fracture model or crack-surface loading. In §2.3.2, we discuss in detail how hydraulic pressure is incorporated in the target value $\mathbf{S}$. The Riemann solutions for the separation case, decorated by S, are then obtained by preserving the characteristic values on each side of the interface,

$$\breve{s}^i_{\mathrm{S}} = \breve{s}^i = S^i \tag{4a}$$

$$\breve{v}^{\pm}_{\mathrm{S}_i} = \breve{v}^{\pm}_i = v_i^{\pm} \pm \frac{S^i - s^{i\pm}}{Z^{i\pm}} \tag{4b}$$

Finally, the solutions for contact–slip mode are obtained by enforcing continuity of normal component of target velocity ($[\![\breve{v}]\!]_1 = 0$). This results in the same solutions for normal direction to that presented in (3). For the tangential directions, target tangential traction components are obtained from Coulomb friction law, resulting in possibly distinct components for tangential velocity target values ($[\![\breve{v}]\!]_i \neq 0$, $i = 2,3$). The solution for tangential directions resemble those for separation mode in (4), with some technical details on how the direction of Coulomb friction is determined. The reader is referred to [11] for detailed derivation and expression for all the Riemann solutions.

2.2 Macroscopic target values and mode regularizations

2.2.1 Macroscopic target values

At any given point at the contact interface Γ the damage parameter D interpolates between *bonded* and *debonded* target solutions,

$$\mathbf{s}^* := (1 - D)\breve{\mathbf{s}}_B + D\breve{\mathbf{s}}_D \tag{5a}$$

$$\mathbf{v}^{*\pm} := (1 - D)\breve{\mathbf{v}}_B + D\breve{\mathbf{v}}^{\pm}_D \tag{5b}$$

where subscripts B and D indicate Riemann values for bonded (*cf.* (3)) and debonded conditions. Note that $\breve{\mathbf{v}}_B$ in (5b) is not decorated with side $\pm$ since from kinematic compatibility condition, same target value is enforced on both sides as evident from (3b). The solution for the debonded part, itself is first divided into contact and separation modes. The relative part of contact to entire debonded $(1 - D)$ fraction, is denoted by η. Finally, the contact mode can take either the contact–stick or contact–slip modes. The number γ denotes the ratio of contact–stick to entire contact fraction. Since the Riemann solutions for bonded and contact–stick modes are the same, *cf.* (3)), there are only the three distinct modes of bonded (B), contact–slip (SL), and separation modes (S). Thus, considering different contact modes within the debonded $(1 - D)$ fraction, the solution (5) can be written as,

$$\mathbf{s}^* := a_{\mathrm{B}}\breve{\mathbf{s}}_{\mathrm{B}} + a_{\mathrm{SL}}\breve{\mathbf{s}}_{\mathrm{SL}} + a_{\mathrm{S}}\breve{\mathbf{s}}_{\mathrm{S}} \tag{6a}$$

$$\mathbf{v}^{*\pm} := a_{\mathrm{B}}\breve{\mathbf{v}}_{\mathrm{B}} + a_{\mathrm{SL}}\breve{\mathbf{v}}^{\pm}_{\mathrm{SL}} + a_{\mathrm{S}}\breve{\mathbf{v}}^{\pm}_{\mathrm{S}} \tag{6b}$$

where

$$a_{\mathrm{B}} = 1 - D + D\eta\gamma \tag{7a}$$

$$a_{\mathrm{SL}} = D\eta(1 - \gamma) \tag{7b}$$

$$a_{\mathrm{S}} = D(1 - \eta) \tag{7c}$$

again in (6b) $\breve{\mathbf{v}}_{\mathrm{B}}$ is not decorated with side notations $\pm$ since from (3b) the stick velocities are the same for both sides.

2.2.2 Determination of D, η, γ

At the top level of hierarchy of relative area fractions, the value of D must be determined. Here we adopt the rate-dependent interfacial damage model of [12,13] where damage rate is given by the evolution law,

$$\dot{D} = \begin{cases} \frac{1}{\tilde{\tau}}[1 - H(\langle D_t - D\rangle)] & D < 1 \\ 0 & D = 1 \end{cases}, \tag{8}$$

$\tilde{\tau}$ is a *relaxation time*, and D_t is the *target damage value*. The function H takes the value of unity at zero and monotonically decreases to 0 at infinity. Following [14],

the particular form of H used in this work is given as $H(x) = \exp(-ax)$. It is evident from (8) that under monotonically increasing quasi-static loading, *i.e.,* load increases much slower than $\tilde{\tau}$, $\langle D_t - D\rangle \to 0$ and $D \to D_t$. That is, D_t is the damage value for the present interface condition, if the loading had been applied under quasi-static condition. The positive part operator in $\langle D_t - D\rangle$ ensures that D is a nondecreasing function of time.

We assume that D_t to be a function of bonded Riemann traction (3a) through a scalar effective stress value $\breve{s}$. One particular choice is $\breve{s} := \sqrt{\langle \breve{s}_{\mathrm{B}}^1\rangle^2 + (\beta \breve{\tau}_{\mathrm{B}})^2}$ for bonded Riemann tangential traction magnitude $\breve{\tau}_{\mathrm{B}} := \sqrt{\sum_{j=2}^{d} \left(\breve{s}_{\mathrm{B}}^j\right)^2}$ and β the *shear stress factor* that controls mode mixity. Finally, D_t is expressed as,

$$D_t = \begin{cases} 0 & \breve{s} < \underline{s}, \\ \frac{\breve{s}-\underline{s}}{\bar{s}-\underline{s}} & \underline{s} \le \breve{s} < \bar{s}\,, \\ 1 & \bar{s} \le \breve{s} \end{cases} \tag{9}$$

where $\underline{s}$ and $\bar{s}$ denote, respectively, effective traction thresholds for the onset of additional damage evolution and for attainment of the maximum damage rate, $1/\tilde{\tau}$. We refer to $\bar{s}$ as the *fracture strength*.

The determination and analysis of η is one of the main emphasis of this paper. In [11], this analysis was provided for $\mathbf{S} = 0$ in (4a). However, that analysis does not carry over to hydraulic fracturing and in general cases when nonzero $\mathbf{S}$ is applied on crack surfaces. The details of the newly proposed approach are provided below. Finally, γ takes the binary values of $\{0, 1\}$ based on whether Coulomb slip condition is satisfied or not, under contact mode. Specifically, $\gamma = 0$ when $|\breve{\tau}_{\mathrm{B}}| > k\left\langle -\breve{s}_{\mathrm{B}}^1\right\rangle_+$ and one otherwise, where k is the friction coefficient.

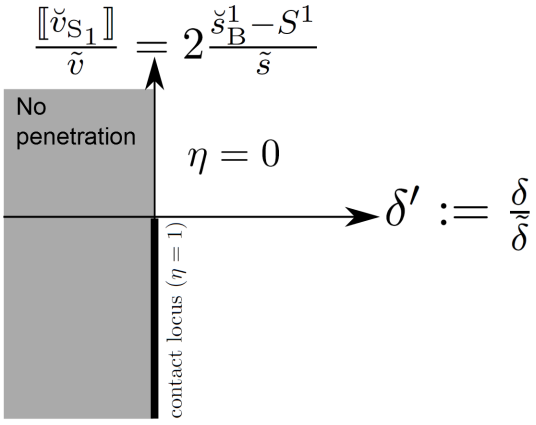

Figure 3: Maps of separation ($\eta = 0$) and contact ($\eta = 1$) modes based on normal separation velocity jump $[\![\breve{v}_{\mathrm{S}_1}]\!]$ and normal displacement jump δ.

Figure (3) shows the 2D phase space for analytical η in terms of nondimensional normal separation velocity jump $[\![\breve{v}_{\mathrm{S}_1}]\!]/\tilde{v}$ and normal displacement jump $\delta' := \delta/\tilde{\delta}$. The fracture scales $\tilde{v}, \tilde{s}, \tilde{\delta}$ are described later. Let u_1^- and u_1^+ be the normal component of displacements from $-$ and $+$ sides. It is clear that the interface is in separation mode ($\eta = 0$) if normal displacement jump $\delta := u_1^- - u_1^+$ is positive. Also, $\delta < 0$ is unacceptable as inter-penetration is not permitted. For $\delta = 0$ the choice on whether contact or separation mode holds depends on the velocity at which the two sides of interface hypothetically separate. To clarify this, among the three modes of bonded (B), contact–slip (SL), and separation (S), it is only the latter that can have nonzero normal displacement jump. Thus, from (6) and (7c) we have,

$$[\![v_1^*]\!] = v_1^{*-} - v_1^{*+} = a_{\mathrm{S}}[\![\breve{v}_1]\!] = D(1-\eta)[\![\breve{v}_{\mathrm{S}_1}]\!] \tag{10}$$

where $[\![\breve{v}_{\mathrm{S}_1}]\!] = \breve{v}_{\mathrm{S}_1}^- - \breve{v}_{\mathrm{S}_1}^+$. Clearly, the value of η has an influence only if $D > 0$, otherwise the interface is fully in bonded mode and as expected from either (5) or (6) $\mathbf{s}^* := \breve{\mathbf{s}}_B$, $\mathbf{v}^* := \breve{\mathbf{v}}_B$. Thus, to determine the value of η when $\delta = 0$ we assume $D > 0$ in (10). If $[\![\breve{v}_{\mathrm{S}_1}]\!] < 0$, then we must have $\eta = 1$; otherwise $[\![v_1^*]\!] < 0$ which is not permissible as it implies interpenetration given that δ is assumed to be zero. On the other hand, if $[\![\breve{v}_{\mathrm{S}_1}]\!] > 0$ from the two choices of $\eta = 0$ and $\eta = 1$, the condition $\eta = 0$ is the physical choice, since it is a positive $[\![\breve{v}_{\mathrm{S}_1}]\!]$ that can take an interface already at contact mode ($\delta = 0$, $[\![\breve{v}_{\mathrm{S}_1}]\!] < 0$) back to separation mode. Thus, for $\delta = 0$, the sign of $[\![\breve{v}_{\mathrm{S}_1}]\!]$ determines η, as shown in (3).

Next, we relate $[\![\breve{v}_{\mathrm{S}_1}]\!]$ to traction quantities which are generally easier to compute, particularly in hydraulic fracturing application. By plugging the values $\breve{v}_{\mathrm{S}_1}^{\pm}$ from (4b) in $[\![\breve{v}_{\mathrm{S}_1}]\!] = \breve{v}_{\mathrm{S}_1}^- - \breve{v}_{\mathrm{S}_1}^+$ and using the identity (3a) we obtain,

$$[\![\breve{v}_{\mathrm{S}_1}]\!] = 2\tilde{Z}^1(\breve{s}_{\mathrm{B}}^1 - S^1) \tag{11}$$

where

$$\tilde{Z}^1 := \frac{2Z^{1-}Z^{1+}}{Z^{1-} + Z^{1+}} \tag{12}$$

is defined as the impedance of the interface for normal waves.

Finally, the quantities in the axes of fig. 3 are normalized by their corresponding fracture scales. This facilitates choosing nondimensional parameters that are used in the regularized version of η, followed shortly. In [15] fracture scales are derived for a general cohesive model. The same analysis can be extended to the damage model with evolution equation (8) to obtain fracture displacement scale $\tilde{\delta}$ and velocity scale $\tilde{v}$,

$$\tilde{\delta} = \frac{\tilde{\tau}\tilde{s}}{\tilde{Z}^1} \tag{13a}$$

$$\tilde{v} = \frac{\tilde{\delta}}{\tilde{\tau}} = \frac{\tilde{s}}{\tilde{Z}^1} \tag{13b}$$

where the stress (strength) scale for the damage model is $\tilde{s} = \bar{s}$ based on the particular form of D_t in (9). Thus, equations (13), (11), and (12) yield the form of normalized axis in fig. 3.

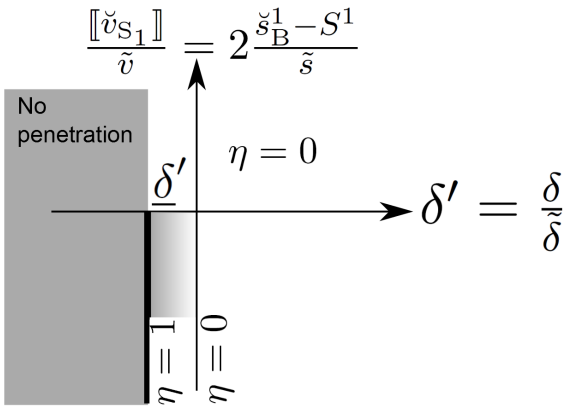

Figure 4: Map of regularized η based on normal separation velocity jump $[\![\breve{v}_{S_1}]\!]$ and normal displacement jump δ.

The binary map of $\eta \in \{0, 1\}$ in fig. 3 cannot be readily used in numerical setting. As described thoroughly in [11], under separation to contact mode transition, there are sudden jumps in both tractions and velocities of the two sides of the interface, as the relative velocity suddenly vanishes and is translated into compressive stress. This necessitates the regularization of η. Figure 4 depicts a regularized version of fig. 3. The parameter $\underline{\delta}' < 0$ denotes the maximum nondimensional penetration permitted in the regularized model, corresponding to displacement jump $\underline{\delta}'\tilde{\delta}$. The particular form of the function that regularizes η from unity to zero for δ' from $-\underline{\delta}'$ to 0 and the exceptionally smooth contact-separation mode transition behavior of this model are described in [11]. Finally unlike cohesive models, this model possesses a maximum penetration which can also be numerically tuned without resulting in a stiff system of equations or nonconvergence issues.

2.3 Application of hydraulic pressure

2.3.1 Pressure factor

By using a simplicial complex representation of cracks and modeling their connectivity by a disjoint set data structure [16], the authors provide a means to transfer hydraulic pressure to an in-situ crack when a hydraulically loaded crack intersects it. This representation, however, only provides information whether a crack is hydraulically loaded or not, resulting in two potential problems. First, if a hydraulically-loaded crack intersects a long crack, clearly not all the points on that crack surface will immediately experience the hydraulic pressure exerted at the connection of the two cracks. Second, similar to separation to contact transition discussed in §2.2.2, traction and velocity fields experience a sudden jump if the full hydraulic pressure is suddenly exerted on newly connected crack surfaces; the in-situ compressive stress between crack surfaces will suddenly jump to a potentially much greater hydraulic pressure if the hydraulic load is immediately transferred. We provide an aperture-based approach that regularizes the transfer of hydraulic load to newly connected crack surface and remedies both aforementioned problems.

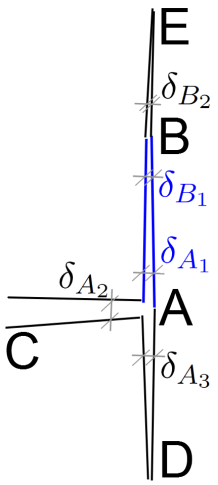

Figure 5: Regularization of the applied hydraulic pressure on a crack surface based on the apertures of connected crack segments.

Figure 5 shows the intersection of a hydraulically loaded crack, segment CA, with an in-situ or otherwise unloaded crack, *i.e.,* the extension of DE. The goal is to regularize the applied hydraulic pressure for the sample segment AB. Accordingly for an arbitrary point P, such as A and B, we define,

$$\delta_{P_{\max}} = \max_i \left(\delta_{P_i}\right) \tag{14}$$

where δ_{P_i} are the apertures of the connected cracks to point P, as shown in the figure for points A and B. Then the *pressure factor* f_p or point P is defined as,

$$f_p(P) = \begin{cases} 0 & \delta'_P \le 0 \\ \frac{\delta'_P}{\bar{\delta}'} & 0 < \delta'_P < \bar{\delta}' \\ 1 & \bar{\delta}' < \delta'_P \end{cases} \tag{15}$$

where $\delta'_P = \delta_{P_{\max}}/\tilde{\delta}$ is the maximum aperture at point P, normalized by displacement scale $\tilde{\delta}$, *cf.* (13a). The nondimensional parameter $0 < \bar{\delta}' \ll 1$ basically regularizes the application of hydraulic load from $\delta_{P_{\max}} = 0$ to $\delta_{P_{\max}} = \bar{\delta}'\tilde{\delta}$.

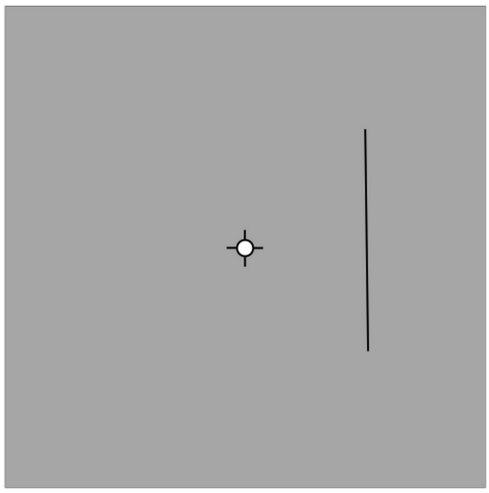

Figure 6: Sketch of four oriented perforations interacting with single natural fracture oriented vertically.

2.3.2 Regularized hydraulic pressure

It is evident from (15) that f_p for a point P tends to one when maximum aperture $\delta_{P_{\max}}$ $\delta_{P_{\max}}$ reaches the threshold value of $\bar{\delta}'\tilde{\delta}$. Pressure factor f_p basically specifies the fraction of hydraulic pressure that is enforced. For the remaining fraction, $1 - f_p$, a target normal traction that would have been active in the absence of hydraulic pressure should be enforced. Accordingly, the normal component of target separation traction, *cf.* (4a) is given by,

$$S^1 = -\left\{ f_p p_h + (1 - f_p)\langle -\check{s}^1_{\mathrm{B}} \rangle \right\} \tag{16}$$

where p_h is the hydraulic pressure at the given space and time position. The second term in the interpolation $\langle -\check{s}^1_{\mathrm{B}} \rangle$ is the compressive traction under bonded (contact) mode. Given that S is one of the three contact modes within debonded part (D fraction) of damage model, *cf.* §2.2.1 and (6a), (5a), the $(1 - f_p)$ part in (16) cannot withstand any tensile traction. The positive part in $\langle -\check{s}^1_{\mathrm{B}} \rangle$ ensures that zero compressive stress in considered when the bonded normal traction is tensile ($\check{s}^1_{\mathrm{B}} > 0$). The front minus sign in (16) is needed to express the regularized compressive traction with tensile positive convention. Finally, in the present work $S^2 = 0$, as it is assumed that no shear traction is applied on crack surfaces through the fluid's viscous effects.

Lastly, we want to investigate under what conditions, the hydraulic pressure p_h is large enough to cause crack opening. When the interface is in (partial) contact condition, which implies $\underline{\delta}' \leq \delta \leq 0$, it transitions to separation mode if and only if $[\![\check{v}_{\mathrm{S}_1}]\!] \geq 0$, as discussed in §2.2.2. By plugging the pressure factor regularized form of S^1 from (16) into (11), it is easy to demonstrate that $[\![\check{v}_{\mathrm{S}_1}]\!] \geq 0$ is equivalent to $p_h \geq -\check{s}^1_{\mathrm{B}}$. This implies that a hydraulically loaded interface in (partial) contact transitions to separation mode if and only if hydraulic pressure is greater than or equal to the ambient pressure. Clearly, this is the physical condition that would been expected in the absence of regularization. That is, the proposed regularization does not affect the physical contact to separation condition and only smoothens it.

3 NUMERICAL EXAMPLES

In the first two examples, presented in §2.3, we demonstrate the need to regularize the application of hydraulic pressure, especially when a hydraulically loaded crack intersects an unloaded crack. The re-fracture example in §3.2 demonstrates that the regularization scheme in §2.2.2 can smoothly model transition between contact and separation modes. We note that the crack path is determined by finding the direction that maximizes the effective stress $\check{s}$, *cf.* (2.2.2); the *h*-adaptive *spacetime Discontinuous Galerkin* method [17] and advanced spacetime adaptive operations [12] are used to solve the underlying elastodynamic problem and allow (hydraulically loaded) cracks to propagate with arbitrary directions dictated by the aforementioned criterion. For reference for all problems, rock is under confining pressure of 2.425 MPa in all directions at initial time and its material properties are: Young's modulus $E = 20$ GPa, mass density $\rho = 2500$ kg/m^3, and Poisson's ratio $\nu = 0.20$. The interface properties are: fracture strength $\bar{s} = 2$ MPa and relaxation time $\tilde{\tau} = 30$ ms.

3.1 Hydraulic pressure regularization

Figure 6 shows the schematic of a problem where a hydraulically loaded fracture intersects a vertically oriented unloaded natural fracture. The hydraulic pressure p_h ramps up from ambient pressure of 2.425 MPa to the sustained value of 19.4 MPa in 1 microseconds. Figure 7a shows the instant at which scattered elastic waves from propagating hydraulic fracture reach the tips of the vertical crack. Figures 7b to 7d show a time period of less than 25 μs where the leading branch of hydraulically loaded cracks intersects the vertical crack. In this problem we intentionally have not regularized the application of hydraulic pressure and have used a short ramp time in the application of hydraulic load to better demonstrate the ensuing problems. First problem is the sudden jump in the pressure exerted on the vertical crack faces. At the time of intersection, which is roughly at 800 μs, hydraulic pressure is $p_h \approx 16$ MPa. That is, upon intersection the pressure instantly jumps from the ambient pressure of 2.425 MPa to $p_h \approx 16$ MPa. The spikes in these figures correspond to a sudden jump in material velocity field induced by instantaneous application of hydraulic load. The second problem is that as shown the entire crack line experiences the hydraulic load right at the time of intersection, *cf.* fig. 7b. Aside from these nonphysical responses, the nonregularized application of hydraulic load results in high levels of mesh adaptivity due to the induced numerical errors. The sharp and spread velocity spikes in figs. 7(b-f) and particularly the high velocity spike near the point of intersection in fig. 7f are some examples of numerical artifacts.

For the second problem we use a parameter $\delta'_P = 0.1$, *cf.* (15), to demonstrate the effect of pressure regularization. Similar to previous problem a horizontal and hydraulically loaded crack intersects an unloaded vertical crack and the hydraulic pressure p_h ramps up from the

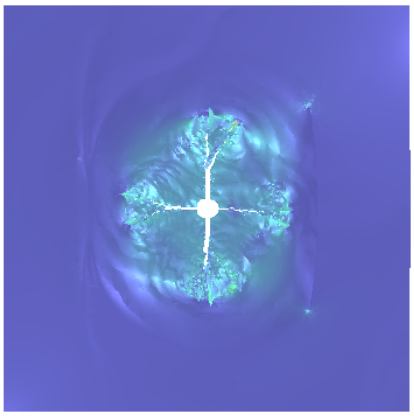

(a) Stage 1.

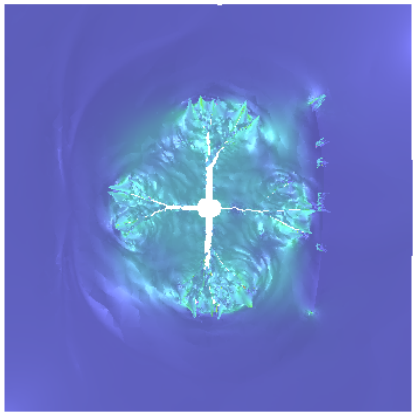

(b) Stage 2.

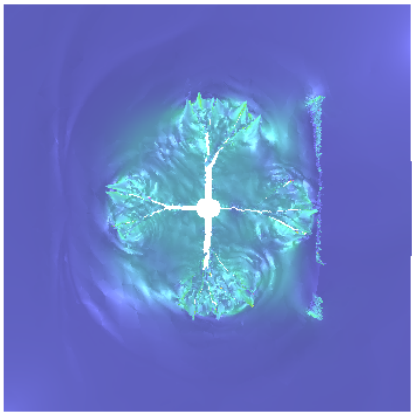

(c) Stage 3.

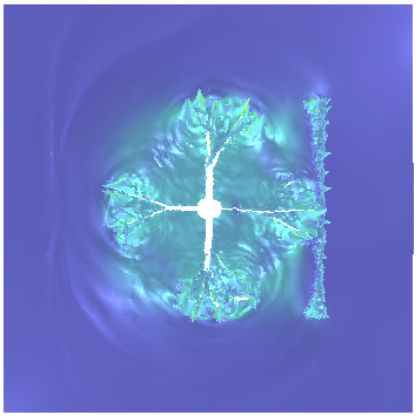

(d) Stage 4.

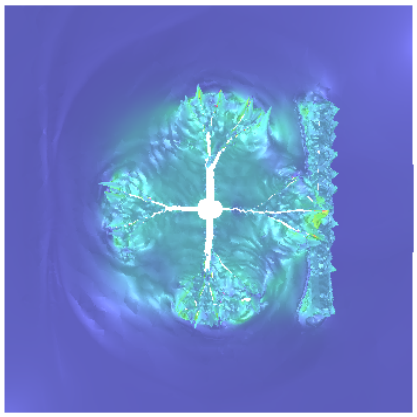

(e) Stage 5.

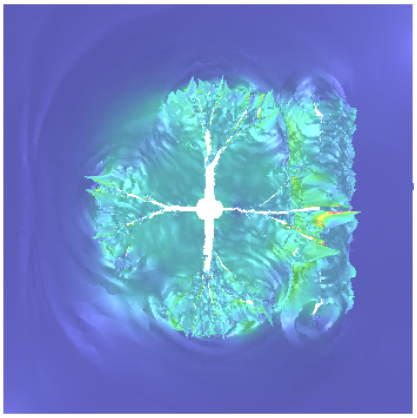

(f) Stage 6.

Figure 7: A sequence of solution visualizations of interaction of a hydraulically-loaded moving crack with an unloaded vertical crack. Lack of pressure regularization results in sharp jumps in stress and velocity. Color and height field depict strain and kinetic energy densities.

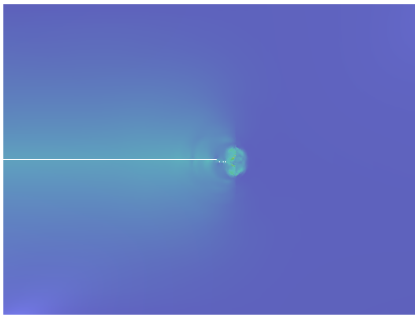

(a) Time $t = 563$ μs

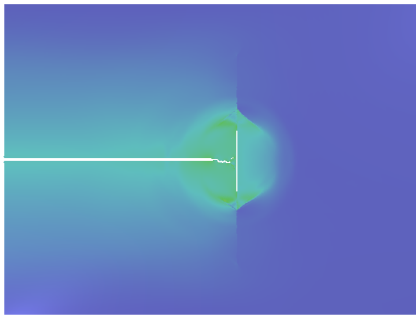

(b) Time $t = 717$ μs

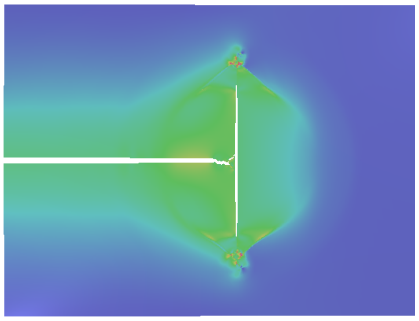

(c) Time $t = 922$ μs

Figure 8: A sequence of solution visualizations for the interaction of a hydraulically-loaded moving crack with an unloaded vertical crack. Color field depicts strain energy density.

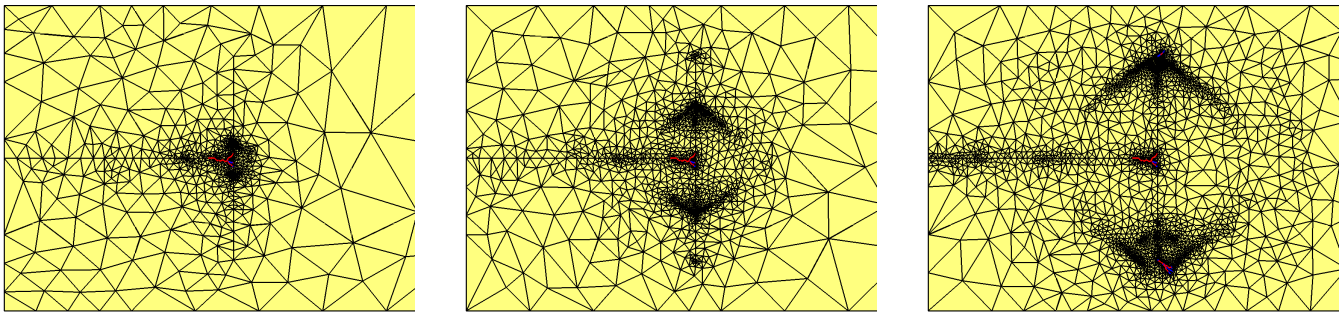

(a) Time $t \approx 563$ μs (b) Time $t \approx 717$ μs (c) Time $t \approx 922$ μs

Figure 9: A sequence of space mesh visualizations for the interaction of a hydraulically-loaded moving crack with an unloaded vertical crack.

ambient pressure of 2.425 MPa to the sustained value of 19.4 MPa in 1 microseconds.

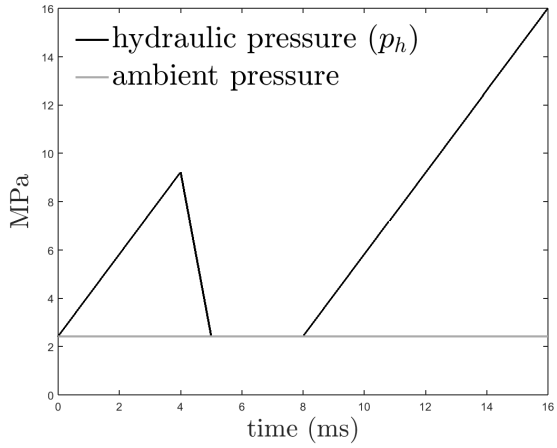

Figure 10: Load history for the hydraulic re-fracturing problem.

Figures 8 and 9 show the strain energy density solutions and the finite element space meshes for three different stages of the problem, respectively. Figures 8a and 9a show a time slightly after the intersection of the cracks. As evident, the regularization eliminates instantaneous loading of the vertical crack and the propagation of the pressure to its entire length.

The next figures show a stage where the hydraulic pressure front has advanced about halfway along the vertical crack. In fig. 8b we observe process zone regions on the vertical crack where the interface transitions from ambient compressive stress state on the outer sides to separation mode induced by the hydraulic pressure. The high level of mesh refinement in these zones in fig. 9b corresponds to high gradients experienced in the values of target compressive traction on the interface. As shown in both figures, the waves emanated from these contact transition points generate waves in the bulk with diagonal fronts. Finally, fig. 8c and fig. 9c correspond to a time slightly after the contact transition point reaches the tips of the vertical crack. The hydraulic load causes the propagation and bifurcation of new cracks off of these tips.

3.2 Contact and re-fracture in hydraulic fracturing

Figure 10 shows the time history of applied hydraulic pressure for a domain with geometry similar to that in fig. 6 but without the vertical crack. The purpose of this example is to demonstrate that the regularization of η from §2.2.2 smoothens the transition of a hydraulically loaded crack from separation to contact mode when hydraulic load is removed and to use the pressure factor concept from §2.3 to gradually re-apply hydraulic pressure on already fractured segments. Similar to previous problems, the loads are applied rapidly to better demonstrate various contact and load transition modes.

Figures 11 and 12 show the SDG solution and space mesh for different stages of this hydraulic re-fracturing problem. In addition, in fig. 12 we map pressure factor f_p to color on fracture segments to discuss its evolution in time. Figures 11a and 12a show the solution and mesh in the early stages of the period when the hydraulic load is being removed. The existence of regions of high kinetic and strain energy densities, mapped to height and color fields respectively, corresponds to a highly transient crack propagation regime. The diagonal short crack between the right and top main cracks propagates in shear mode and is not hydraulically loaded; *cf.* fig. 12a where $f_p = 0$. The propagation of this crack is induced by scattered waves and stress redistribution. Other than this, all the other cracks are hydraulically loaded and propagate in a tensile-dominated mode.

Figures 11b and 12b correspond to $t = 5$ ms where the hydraulic pressure is completely removed. As a result, we already observe some microcracks start to transition to contact mode with the microcrack on the top left side of the vertical main crack being one example. The figures 11(c-d) and 12(c-d) refer to times slightly after the removal of the hydraulic load. We observe that the crack surfaces start to close. See for example the closure of the horizontal crack segment at the far left end of the left main crack. Local wave scattering events and the transition of f_p to zero can be seen in figs. 11c and 12c. Another interesting observation is the emittance of acoustic waves in all directions as a result of crack and microcrack closures. The front of these secondary waves can more clearly be seen in figs. 11d and 12d.

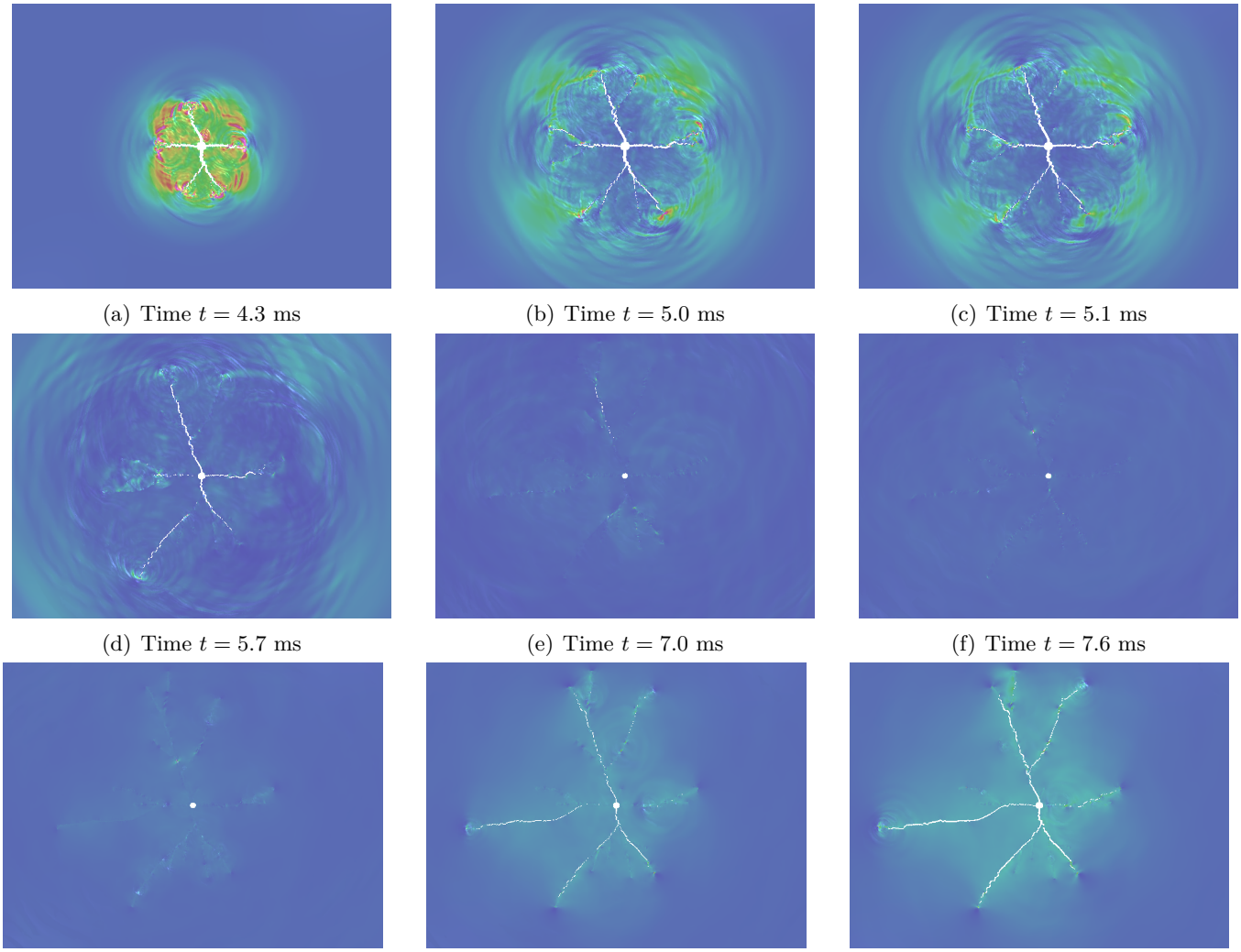

(a) Time $t = 4.3$ ms (b) Time $t = 5.0$ ms (c) Time $t = 5.1$ ms

(d) Time $t = 5.7$ ms (e) Time $t = 7.0$ ms (f) Time $t = 7.6$ ms

(g) Time $t = 8.6$ ms (h) Time $t = 9.2$ ms (i) Time $t = 9.5$ ms

Figure 11: A Sequence of solution visualizations for the hydraulic re-fracturing problem. Color and height field depict strain and kinetic energy densities.

Figures 11(e-f) and 12(e-f) show the transition of the remaining crack surfaces to contact mode. The progression of regions with complete crack closure and $f_p = 0$ can be observed in the figures. It should be emphasized that the regularization of η, *cf.* fig. 4, is essential in smooth separation to contact mode transition. Also, the low level of mesh refinement in fig. 12(e-f), compared to previous times, stems from the fact that the entire domain is reverting to its spatially uniform ambient pressure field.

Finally, in figs. 11(g-i) and 12(g-i) the cracks start to transition back to separation mode after the start of the second stage of hydraulic loading from time $t = 8$ ms. Specifically, in the space meshes we observe the progression of f_p from zero to one for all cracks except a few microcracks that remain arrested and in contact. As expected, cracks further open and propagate in tensile-dominated mode due to hydraulic loading. One key aspect of the model for transition from contact to separation mode is the use of the aperture of all connected segments to a crack segment, rather than only the crack itself (that is using cracks CA, BE, and AD in fig. 5 in computing f_p for crack segment AB), in computing $\delta_{P_{\max}}$ in (14) and subsequently f_p in (15). This results in natural propagation and re-application of hydraulic load from the main four initial perforations outward to other cracks. Otherwise, all crack segments would remain in contact mode given that their opening does not increase in the absence of hydraulic pressure.

4 CONCLUSIONS

We presented an interfacial damage model for hydraulic fracturing applications that can seamlessly combine separation, contact–stick, and contact–separation modes. Examples from crack intersection and re-fracturing demonstrated the capabilities of the proposed separation to contact regularization and aperture-based hydraulic pressure regularization schemes. They enable smooth transfer of hydraulic load to a newly intersected crack and smoothen contact mode transition upon the application or removal of hydraulic pressure. Finally, we note that if hydraulic pressure is obtained from a more physical model, the concept of pressure factor may no longer be needed. For example, once the connectivity of a crack to a hydraulically loaded crack is determined from simplicial complex ap-

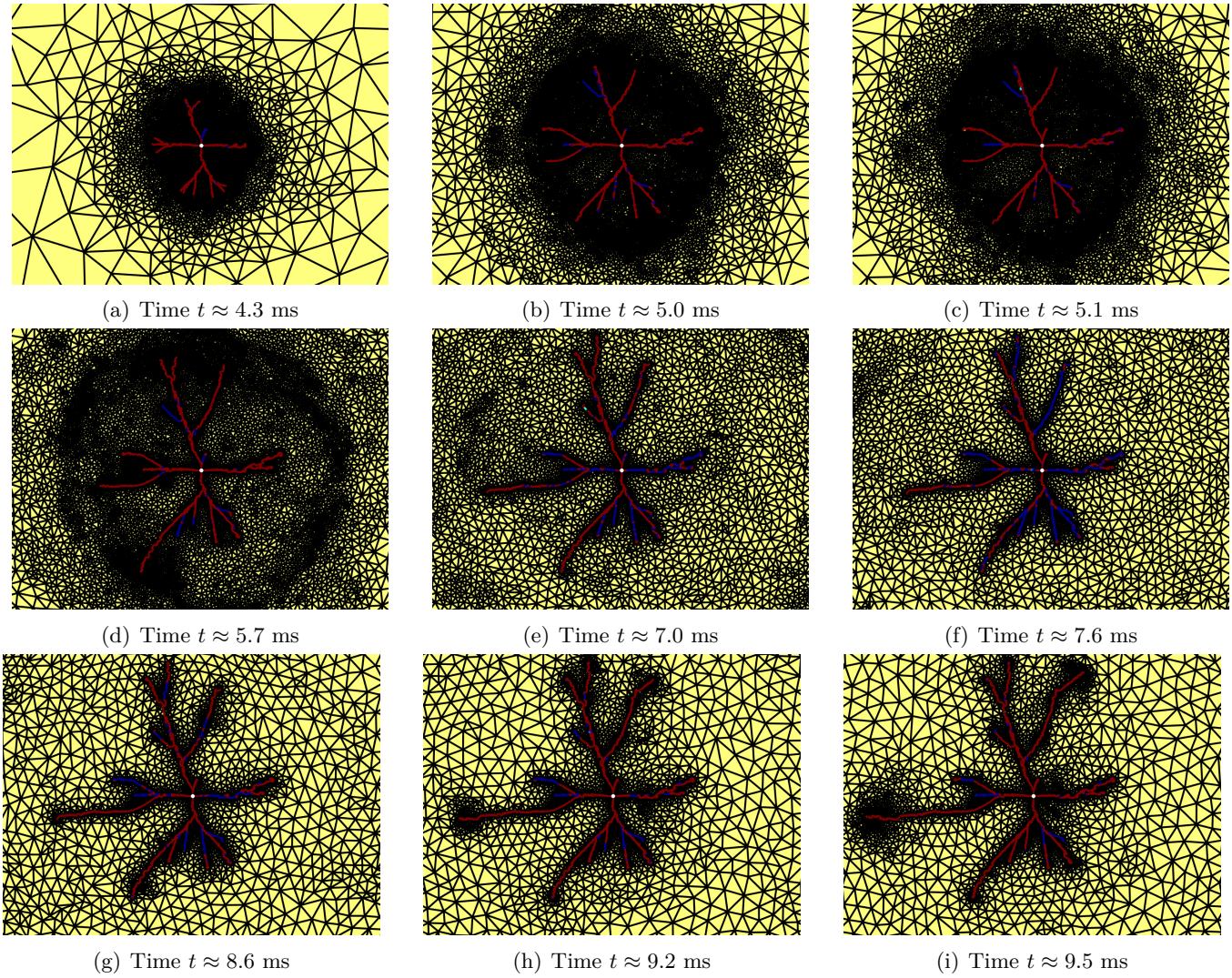

(a) Time $t \approx 4.3$ ms (b) Time $t \approx 5.0$ ms (c) Time $t \approx 5.1$ ms

(d) Time $t \approx 5.7$ ms (e) Time $t \approx 7.0$ ms (f) Time $t \approx 7.6$ ms

(g) Time $t \approx 8.6$ ms (h) Time $t \approx 9.2$ ms (i) Time $t \approx 9.5$ ms

Figure 12: A Sequence of space mesh visualizations for the hydraulic re-fracturing problem. Crack segments are colored based on the value of pressure factor f_p with blue to red corresponding to the range $f_p \in [0\ 1]$.

proach in [16], the aperture-dependent pressure from lubrication equation may already smoothen the transition of hydraulic load to a new crack.

REFERENCES

[1] Taleghani, Arash Dahi, Miguel Gonzalez, and Amir Shojaei (2016) Overview of numerical models for interactions between hydraulic fractures and natural fractures: Challenges and limitations. *Computers and Geotechnics*, **71**, 361–368.

[2] Huang, Bingxiang, Changyou Liu, Junhui Fu, and Hui Guan (2011) Hydraulic fracturing after water pressure control blasting for increased fracturing. *International Journal of Rock Mechanics and Mining Sciences*, **48**, 976–83.

[3] Mohammadnejad, T. and J.E. Andrade (2016) Numerical modeling of hydraulic fracture propagation, closure and reopening using XFEM with application to in-situ stress estimation. *International Journal for Numerical and Analytical Methods in Geomechanics*, **40**, 2033–2060.

[4] Eshkalak, Mohammad O, Umut Aybar, Kamy Sepehrnoori, et al. (2014) An economic evaluation on the re-fracturing treatment of the US shale gas resources. *SPE Eastern Regional Meeting*, Society of Petroleum Engineers.

[5] Wriggers, P., T. Vu Van, and E. Stein (1990) Finite element formulation of large deformation impact-contact problems with friction. *Computers and Structures*, **37**, 319 – 331.

[6] Kikuchi, Noboru (1982) A smoothing technique for reduced integration penalty methods in contact problems. *International Journal for Numerical Methods in Engineering*, **18**, 343 – 350.

[7] Hughes, T.J.R., R.L. Taylor, J.L. Sackman, A. Curnier, and W. Kanoknukulchai (1976) A finite element method for a class of contact-impact problems. *Computer Methods in Applied Mechanics and Engineering*, **8**, 249 – 276.

[8] Simo, J.C., P. Wriggers, and R.L. Taylor (1985) A perturbed lagrangian formulation for the finite element solution of contact problems. *Computer Methods in Applied Mechanics and Engineering*, **50**, 163 – 180.

[9] Faivre, M., B. Paul, F. Golfier, R. Giot, P. Massin, and D. Colombo (2016) 2D coupled HM-XFEM modeling with cohesive zone model and applications to fluid-driven fracture network. *Engineering Fracture Mechanics*, **159**, 115–143.

[10] Cirak, Fehmi and Matthew West (2005) Decomposition contact response (DCR) for explicit finite element dynamics. *International Journal for Numerical Methods in Engineering*, **64**, 1078 – 1110.

[11] Abedi, Reza and Robert B. Haber (2014) Riemann solutions and spacetime discontinuous Galerkin method for linear elastodynamic contact. *Computer Methods in Applied Mechanics and Engineering*, **270**, 150 – 177.

[12] Abedi, Reza (2010) *Spacetime damage-based cohesive model for elastodynamic fracture with dynamic contact*. Ph.D. thesis, Department of Theoretical and Applied Mechanics, University of Illinois at Urbana–Champaign.

[13] Omidi, Omid, Reza Abedi, and Saeid Enayatpour (2015) An adaptive meshing approach to capture hydraulic fracturing. *The 49th US Rock Mechanics/Geomechanics Symposium, June 28-July 1, San Francisco,CA,USA*.

[14] Allix, O. and A. Corigliano (1996) Modeling and simulation of crack propagation in mixed modes interlaminar fracture. *International Journal of Fracture*, **77**, 111–140.

[15] Abedi, R. and R.B. Haber (2011) Spacetime dimensional analysis and self-similar solutions of linear elastodynamics and cohesive dynamic fracture. *International Journal of Solids and Structures*, **48**, 2076 – 2087.

[16] Clarke, P.L., O. Omidi, and R. Abedi (2016) Modeling crack connectivity of induced fractures in a naturally fractured formation. *Proceeding: 50th US Rock Mechanics/Geomechanics Symposium, June 26-June 29, Houston, Texas - USA*, pp. ARMA 16–0532 (13 pages).

[17] Abedi, Reza, Robert B. Haber, and Boris Petracovici (2006) A spacetime discontinuous Galerkin method for elastodynamics with element-level balance of linear momentum. *Computer Methods in Applied Mechanics and Engineering*, **195**, 3247–3273.